Mathematical Modelling and Numerical Simulation with Applications, 2024, 4(4), 416–447

https://dergipark.org.tr/en/pub/mmnsa
ISSN Online: 2791-8564 / Open Access
https://doi.org/10.53391/mmnsa.1536174

RESEARCH PAPER

Two-phase MHD peristaltic flow of non-Newtonian Casson fluid through the renal tube in the presence of microliths

P. Deepalakshmi [1,‡], **E. P. Siva** [1,*,‡] **and K. Loganathan** [2,‡]

[1]Department of Mathematics, College of Engineering and Technology, SRM Institute of Science and Technology, Kattankulathur-603203, Tamil Nadu, India, [2]Department of Mathematics and Statistics, Manipal University Jaipur, Jaipur-303007, Rajasthan, India

*Corresponding Author
‡dp5497@srmist.edu.in (P. Deepalakshmi); sivae@srmist.edu.in (E. P. Siva); loganathankaruppusamy304@gmail.com (K. Loganathan)

Abstract

The ureter regulates urine flow and has one to five peristaltic contractions per minute. Understanding this fluid dynamics is crucial for improving treatments, especially for chronic kidney disease (CKD). Investigating the peristaltic motion of a Casson fluid with suspended particles is essential for improving urological treatments and developing effective interventions. The core part of the article expresses the flow pattern of urine with debris in the urine stream which interrupt the flow within the ureter. The novelty of the current research lies in the simultaneous consideration of various factors that have not been previously explored in peristaltic urological transport. The results declare that the drag particulate suspension parameter (ζ) has a decelerating impact on the velocity of the particles while simultaneously accelerating the velocity of the fluid phase. Increased C leads to a notable decrease in the temperature of the fluid phase, while a rise in both the Eckert number (Ec) and Saffman suspension parameters (ζ) results in an inclination in temperature in the peristaltic regime. This research is relevant for conducting heat-dose sensitivity tests, which are essential for effective CKD treatment.

Keywords: Computational fluid dynamics; peristalsis; thermal radiation; trapping bolus; ureteral flow

AMS 2020 Classification: 34B15; 35C05; 76A05; 76D05; 80A21

1 Introduction

In this ultra-speed development of mathematical modelling in various kinds of fluid flow with peristalsis, the advancement of the two-phase flow in mathematical aspects has been concerned. Most of the fluid flows have a core application, particularly in the optimisation of products, because they require prominent knowledge of fluid flow patterns and behavior. Among these, the two-phase flow has a crucial application in clinical treatments rather than engineering aspects.

➤ **Received:** 20.08.2024 ➤ **Revised:** 20.10.2024 ➤ **Accepted:** 07.11.2024 ➤ **Published:** 30.12.2024

The potential application of two-phase flow in biology is in microfluidics, which is the study of fluid flow in small channels and devices. Two-phase flow is commonly used in microfluidic devices for manipulating and analysing cells and particles. It is more effective while taking Magnetic Resonance Imaging (MRI) by injecting a contrast agent into the bloodstream, which creates a two-phase system inside the blood and is also helpful in the separation and purification of biological materials. Here it is taken into consideration because of its role in the sedimentation of particles in fluid flow, such as alluviation calculi in the ureter, stenosis in blood capillaries, and obstructions in the pulmonary valve, lumbar region, esophagus, trachea, etc. The novelty of the problem is analysing wall properties in the presence of peristaltic, two-phase flow in between the coaxial tubes of the ureter. Peristalsis has its dominant objective in the urinary system, which creates an involuntary sinusoidal muscular shrinkage of the uterine wall, which pushes the urine from the kidney to the urinary bladder via wavy tubes of the ureter. Lozano [1] explored the problem of ureteral peristaltic motion with particle trajectories, and certain parameters of the fluid phase insist that reflux might occur next to the walls. An experimental lecture by Kiil [2] delivered the response of dilatation obviously happening in the ureteral wall during catheter insertion to record the ureteral activity. Vahidi et al. [3] demonstrated the physical nature of wall compliance in ureter, the peak level of contraction wave and also the stress tension at the ureteric wall. Thus, it revealed a new approach to evaluating peristaltic mechanism in an accurate manner.

The consecutive motion of sinusoidal waves induces the transport of substances inside a tube or channel, a process typically referred to as the peristaltic mechanism. Srivastava et al. [4] constructed a modern methodology of analysing peristaltic mechanism in two-phase flow (i.e., Particle-fluid mixtures). They evaluated the results of velocity using momentum equations in both phases and made comparisons between them. This depicts the reduction of fluid velocity in the axial direction when there is an increment in the solute concentration. The system of governing equations for both fluid and particle phases has been considered and explained properly. On taking reference to the paper, Kamal et al. [5] framed the system of equations as implying particle suspension in the boundless parallel type of walls with major mention of the sinusoidal wave with slip condition. Their validated graphs indicate that the critical value of the pressure gradient is relatively lower when particle motion occurs in the fluid compared to free flow. The role of muscular expansion due to peristaltic motion gives a better statement of analysis with slip condition. A deep discussion was made on the hydrodynamics flow of RBC (Red Blood Cells) in micropump affected by hall current and slip effects spoken by Ramesh et al. [6]. The transformed governing equations indicate two-phase flow both particle and fluid separately. Slip conditions enhance bolus magnitudes. The major conclusion of the chosen modelling equations incorporated has been solved by exact solutions. They accelerate the flow very close to the channel walls. The Particle depositions inside the cylindrical tube have a vital application in the excretion of urine waste from the urethra. Misra and Pandey [7] justified the obstructions are trapped in the middle of contracted segments of urinary flow through ureter. In this segment, the mechanism of peristalsis widely helps ureter for pushing out urine through the urethra. They recommended the theory of declinement in pumping efficiency of ureter suppresses the quantity of urine excretion. Kasim [8] and Maraj et al. [9] transformed a nonlinear system of equations for both phases, solving them to analyze the physical significance of the resulting graphs, which were generated by applying various parameters. They picturized the magnification of velocity in raising the suspension of particles by the influence of the Casson model.

To the best of our knowledge, there have been no attempts made to study the Eyring-Powell tensor's peristaltic system in the presence of solid particles flowing along a curved channel, as investigated by Riaz and Sadiq [10]. The problem formulation can be recognised as steady by employing a lubricating approach that converts unsteady coordinates into wave frame coordinates.

The discharge of liquid and solid mixtures, flow rates, pressure gradient, and pressure increase also have been discovered. They assembled the system of dimensionless structure of equations with demonstrated conditions. The equations derived were analyzed using lubrication constraints, and then a perturbation strategy was applied. The physical representation of the governing model illustrates the relationship between flow rates and pressure gradients. The curved passage may reduce the pressure gradient as fluid flows through it. Hayat et al. [11] explored thermophoresis, also known as the Soret effect, which is utilized in industry to separate large and small molecules from their solution in thermal field flow fractionation (TFFF). This is advantageous for dealing with biological samples such as cells, proteins, and DNA, as significant fluctuations in temperature might cause the samples to disintegrate. In addition, some industrial procedures encompassed the Haber process, which involves chemically extracting nitrogen from the air to produce ammonia, and disinfection, which refers to the chemical treatment used to eliminate germs and viruses, which involves the chemical combination of materials such as cement. They examined the impact of Joule heating and chemical reactions in a peristaltically driven Casson non-Newtonian fluid by incorporating various influences. An alternative fundamental study coupled stress parameter coined by Zhang et al. [12] explained the heat and mass transfer in a genuine way. Past investigations portrayed invariably single-phase fluid flow. When dusty particles are added then fluid becomes two-phase flow. Thus Bhatti et al. [13] examined the flow characteristics with the influence of two potential forces including electrical and magnetic forces. Bhatti et al. [14], approached a particular theory called lubrication to derive the proposed model in the wavy channels along with significant effects. Among many physiological fluids couple stress fluid is taken for consideration for the outcome of its best applications. The typical phenomena of physiological fluid are reflux and trapping which is drafted first by Kaimal [15]. This inspection accounting to find out the changes in density and viscosity of suspended particles. Sankad and Nagathan [16] had witnessed the heat transfer impact while considering wall slip effects during progressive motion of fluid. Modelling of dusty water is figured out by Ramesh et al. [17]. The complexity of the chosen model has its impact on thermal radiation. They presented a flow characteristic in a two-phase boundary layer formed around the rotating round-nosed body. This contamination requires effective surface heating to purify dusty particles. Hayat et al. [18] worked significantly to impose heat and mass transfer effects in Sutterby fluid.

A numerical approach for deriving mathematical modelling of third-grade fluid was executed by Prakash et al. [19]. A detailed view of pressure rise, shear stress amplitude and flow parameter variations are given by them. Here the Casson fluid is taken into account because for its shear thinning and shear thickening behaviour. This fluid may be attributed to dislocation of structural elements leading to declinement of viscosity. In the other case, when shear thickening emerges the structural elements will resist the flow, resulting in the enhancement in viscosity of the fluid. Javed et al. [20] numerically analysed the behaviour of magnetohydrodynamic Casson fluid in peristaltic flow. They specifically focus on exploring the unexplored features of peristaltic motion by taking into account the assumptions of long wavelength and low Reynolds number. The suitability of Casson fluid for the blood flow model is a well-established fact. The utilisation of Casson modelling by Mernone et al. [21] was suitable as it has the potential to provide understanding regarding the accuracy of simplifying the modelling process for particular non-Newtonian fluids, such as the flow of urine in the ureter and blood flow in the blood arteries, under specific physiological circumstances. Bhatti et al. [22] examined the transmission of heat and mass in the presence of magnetic field-induced peristaltic motion of solid particles in a dusty Casson fluid. The study also considered the effects of nonlinear thermal radiation and the Hall effect. Eldabe et al. [23] explored the axial velocity, temperature, and concentration distributions are determined based on the fluid characteristics. Visual demonstration of the impact of different parameters on

these solutions explained using a series of figures. They executed the explicit finite difference method to solve the equations governing velocity, heat, and concentration.
Mekheimer et al. [24] and Naveed et al. [25] have shown their novel contribution to the peristaltic motion of Newtonian behaviour of fluids. The flow passage is considered as a planar channel. The manuscript with the modelling is solved using perturbation series. In this survey, numerous researchers examined the field of peristaltic flow and their behaviour in different physical situations. The current study by Kothandapani and Srinivas [26] can be applied to the peristaltic transfer of intra-uterine fluid through a porous material. A meticulous comparison is conducted among four distinct wave patterns in the context of a symmetrical porous channel. The study also investigated the impact of various relevant factors on the stream function and pressure drop. Prakash et al. [27] have provided a theoretical study on the peristaltic radiative-convective dissipative magnetohydrodynamic electro-osmotic propulsive flow of a viscous nano-liquid in an asymmetric microchannel. The combined effects of both axial electrical field and a transverse magnetic field have been investigated by them. The model incorporates convective boundary conditions as well as the impacts of heat sources and sinks. The study conducted by Kothandapani and Prakash [28] focused on the investigation of radiation heat transport in porous materials.
The introduction of wall properties and their importance are spoken well by Bhatti et al. [29]. Perturbation technique plays a vital role in solving and plotting of flow rate. Wall rigidity, stiffness, and damping nature are the factors discussed in the graphs. This research has significant applications in both biological and industrial sectors. The fluid taken for transport is compressible. Their particular study discloses the compressibility of taken fluid, features of the wall related to particle motion, slip effects, and heat transmission in the availability of peristaltic pumping.
The thermal radiation parameter, as elucidated by Prakash et al. [30] has been considered. In order to analyze the impacts of thermal radiation, a thermal radiative flux model is utilized. The governing equations have been formulated and subsequently simplified using lubrication theory. The impact of different parameters on the transport characteristics has been investigated through computational illustrations. Lozano et al. [31], Prakash et al. [32] and Shankar et al. [33] have given an examination of the axisymmetric peristaltic flow of a mixture of solid and liquid in the ureter. The findings provided insights into the mechanisms of ureteral peristalsis when solid particles are present, such as in the case of ureteral lithiasis. The governing partial differential equations are analytically transformed into nonlinear ordinary differential equations through a systematic procedure by Deepalakshmi et al. [34] and Eroğlu [35]. The homotopy analysis method for solving equations has been applied by Loganathan et al. [36] and Sinan et al. [37]. The findings provided insights into the mechanisms of ureteral peristalsis when solid particles are present, such as in the case of ureteral lithiasis. The study of renal tube dynamics and the phenomenon of fluid flow through these structures is motivated by several important factors, especially within the field of biomechanics and biofluid mechanics. The renal tubes, like the ureters, play a critical role in the transport of urine from the kidneys to the bladder, a process heavily influenced by both mechanical and fluid dynamic factors. The current work is majorly focusing on the Particle-Fluid suspension with the transporting fluid called Casson fluid. This manuscript quantitatively analyses the transfer effects under the impact of peristaltic motion. The governing equations depict the non-linearity of both Particles and Fluids separately. Those are converted into a dimensionless format with the help of lubrication theory followed by numerical procedure via the DSolve function in Matlab software to estimate the temperature, contour pattern, velocity, and mass transfer of the deposited particles and fluid. The primary purpose is to investigate how peristaltic motion, fluid properties, and external magnetic fields influence the transport of particles in the renal tube, which will contribute to the development of more effective interventions for conditions like kidney stones and CKD. This text highlights several novel aspects of the dynamics

of the ureter in two-phase conditions, which are relevant to the usage of magnetic therapy and thermal radiation techniques. This topic conveys the ureter flow accompanied by particles. The graphical visualizations incorporate the results for various pertinent parameters included in this study. Velocity, temperature, concentration, pressure gradient, streamline, and isotherms have been assessed using analytical techniques. The findings of the present study will be useful and beneficial in physiological processes and will be helpful in better understanding the ureter flow.

2 Mathematical modeling of the problem

This study assumes that the urine exhibits characteristics of homogeneity, non-Newtonian fluid behaviour, viscosity, and incompressibility. The fluid flow problems presented in this study can be characterized by employing the principles of conservation of mass and momentum equations.

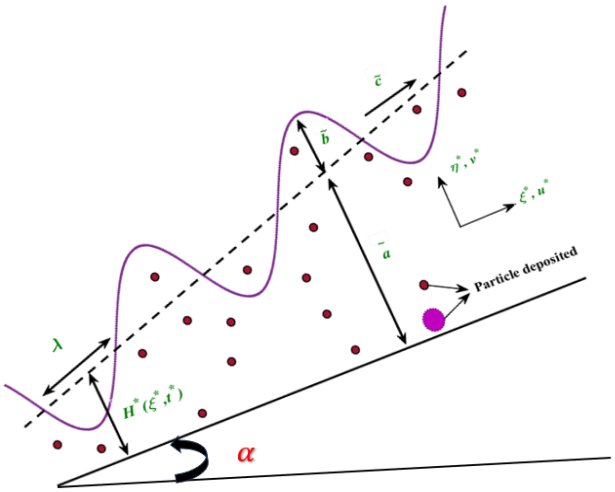

Figure 1. The internal picture of the kidney with ureteral stones

The sinusoidal wave of amplitude $\tilde{b}$, t^* symbolizes the time, $\tilde{K}$ represents the channel's length-dependent constant, wavelength λ, the channel's half-width at the inlet is denoted by $\tilde{a}$, whereas constant velocity $\bar{c}$ travels along the channel wall $H^*\left(\xi^*, t^*\right)$ defined as:

$$H^*\left(\xi^*, t^*\right) = \tilde{a}\sin\left[\frac{2\Pi}{\lambda}\left(\xi^* - \tilde{c}t^*\right)\right] + \tilde{b} + \tilde{K}\xi^*. \tag{1}$$

The physical model under investigation is illustrated with the depiction of the feed mechanism through the kidneys to the ureter may be seen in Figure 1. In accordance with the principles of a Cartesian coordinate system, the ξ^*-axis is defined as the horizontal direction along which a wave propagates, while the η^*-axis is defined as the vertical direction, as depicted in Figure 1. The velocity components of a Casson fluid along the ξ^* and η^* directions in a rectangular coordinate system are denoted as u_f^* and v_f^*.

Expressions for fluid and particle phase

The Physical flow problem constructed via mathematical modelling is taken into account as follows [9, 14]. In the context of two-dimensional Cartesian coordinates, the Navier-Stokes equations can be mathematically expressed as Eqs. (2)-(5),

Fluid-Phase

$$\left[u_f^*\frac{\partial u_f^*}{\partial \xi^*}+v_f^*\frac{\partial u_f^*}{\partial \eta^*}+\frac{\partial u_f^*}{\partial t^*}\right] = -\frac{1}{\rho}\frac{\partial P^*}{\partial \xi^*}+\nu\left(1+\frac{1}{\beta^*}\right)\left(\frac{\partial^2 u_f^*}{\partial \xi^{*2}}+\frac{\partial^2 u_f^*}{\partial \eta^{*2}}\right)+\frac{g\beta_T(T_f^*-T_o^*)sin\alpha}{(1-C)} - \frac{CN}{\rho(1-C)}\left(u_f^*-u_p^*\right)-\frac{\sigma^*\beta_0^2 u_f^*}{\rho(1-C)}, \tag{2}$$

$$\left[u_f^*\frac{\partial v_f^*}{\partial \xi^*}+v_f^*\frac{\partial v_f^*}{\partial \eta^*}+\frac{\partial v_f^*}{\partial t^*}\right] = -\frac{1}{\rho}\frac{\partial P^*}{\partial \eta^*}+\nu\left(1+\frac{1}{\beta^*}\right)\left(\frac{\partial^2 v_f^*}{\partial \xi^{*2}}+\frac{\partial^2 v_f^*}{\partial \eta^{*2}}\right)-\frac{g\beta_T(T_f^*-T_o^*)cos\alpha}{(1-C)} - \frac{CN}{\rho(1-C)}\left(v_f^*-v_p^*\right), \tag{3}$$

$$(\rho c_p)\left[u_f^*\frac{\partial T_f^*}{\partial \xi^*}+v_f^*\frac{\partial T_f^*}{\partial \eta^*}+\frac{\partial T_f^*}{\partial t^*}\right] = K\left(\frac{\partial^2 T_f^*}{\partial \xi^{*2}}+\frac{\partial^2 T_f^*}{\partial \eta^{*2}}\right)+\frac{CN}{(1-C)}(u_f^*-u_p^*)^2 + \frac{\rho_p c_p C}{(1-C)\omega_{\tilde{T}}}(T_f^*-T_p^*)-\frac{1}{(1-C)}\frac{\partial q_r}{\partial \eta^*}, \tag{4}$$

$$\left[u_f^*\frac{\partial K_f^*}{\partial \xi^*}+v_f^*\frac{\partial K_f^*}{\partial \eta^*}+\frac{\partial K_f^*}{\partial t^*}\right] = D_m\left(\frac{\partial^2 K_f^*}{\partial \xi^{*2}}+\frac{\partial^2 K_f^*}{\partial \eta^{*2}}\right)-\frac{\rho_p C}{\rho_f \omega_{\tilde{K}}(1-C)}(K_f^*-K_p^*) + \frac{D_m}{T_0^*}K_{\tilde{T}}\left(\frac{\partial^2 T_f^*}{\partial \xi^{*2}}+\frac{\partial^2 T_f^*}{\partial \eta^{*2}}\right)-E^*(K_f^*-K_0^*). \tag{5}$$

In the aforementioned equations, the variable K represents the thermal conductivity, D_m is the coefficient of mass diffusivity, c_p is specific heat, whereas T_f^*, T_p^* and K_f^*, K_p^* denote the temperature and concentration terms for particles and fluid, respectively. The preceding Eqs. (6)-(9) represent the density ρ, pressure P, the suspension parameter ζ, the drag force N, and the particle volume fraction C.

Particle Phase:

$$\left[u_p^*\frac{\partial u_p^*}{\partial \xi^*}+v_p^*\frac{\partial u_p^*}{\partial \eta^*}+\frac{\partial u_p^*}{\partial t^*}\right] = -\frac{1}{\rho_p}\frac{\partial P^*}{\partial \xi^*}+\frac{N}{\rho_p}\left(u_f^*-u_p^*\right), \tag{6}$$

$$\left[v_p^*\frac{\partial v_p^*}{\partial \xi^*}+v_p^*\frac{\partial v_p^*}{\partial \eta^*}+\frac{\partial v_p^*}{\partial t^*}\right] = -\frac{1}{\rho_p}\frac{\partial P^*}{\partial \eta^*}+\frac{N}{\rho_p}\left(v_f^*-v_p^*\right), \tag{7}$$

$$\rho_p C c_p\left[u_p^*\frac{\partial T_p^*}{\partial \xi^*}+v_p^*\frac{\partial T_p^*}{\partial \eta^*}+\frac{\partial T_p^*}{\partial t^*}\right] = \frac{C\rho_p c_p}{\omega_{\tilde{T}}}(T_f^*-T_p^*), \tag{8}$$

$$\left[u_p^*\frac{\partial K_p^*}{\partial \xi^*}+v_p^*\frac{\partial K_p^*}{\partial \eta^*}+\frac{\partial K_p^*}{\partial t^*}\right] = \frac{1}{\omega_{\tilde{K}}}(K_f^*-K_p^*), \tag{9}$$

where the subscript lying in equations f and p stands for fluid and solid granules. The evaluation is conducted on extra stress tensor β^*, incompressible, solid-liquid Casson non-Newtonian fluid, with regard to momentum and heat flow. Particle velocities represented as u_p^* and v_p^*. The stress tensor S_{ij} is the minimal stress needed to initiate the Casson fluid flow. It is presented in the

following expression

$$S_{ij} = \begin{cases} 2\left(\mu + \frac{P_y}{\sqrt{2\pi}}\right) e_{i,j} & \text{for} \quad \pi \geq \pi_c, \\ 2\left(\mu + \frac{P_y}{\sqrt{2\pi}}\right) e_{i,j} & \text{for} \quad \pi < \pi_c. \end{cases} \tag{10}$$

Introducing non-dimensional parameter $\beta^* = \frac{\mu\sqrt{2\pi}}{P_y}$. Here P_y is the yield stress of Casson fluid, μ is the plastic dynamic viscosity and π indicates the multiplication of the component of deformation rate with itself ($\pi = e_{ij}.e_{ij}$), and π_c represents the crucial value according to the Casson fluid model. For the scenario where the value of $\pi > \pi_c$ in the context of a Casson fluid model.
The drag coefficient and classical Stoke's drag equation are defined as,

$$S^* = \frac{9\mu_s}{2\tilde{a}^2}\lambda(C), \tag{11}$$

$$\lambda(C) = \frac{4 + 3\sqrt{8C - 3C^2} + 3C}{4 - 12C + 9C^2}. \tag{12}$$

According to Srivastava [38], the viscosity of the suspension does not follow Einstein's equation when C exceeds 0.05. Then the suspension is represented as:

$$\mu_0 = \frac{\mu_s}{(1 - \beta C)}, \tag{13}$$

$$\beta = \frac{70}{100} exp\left[\frac{249}{100}C + \frac{1107}{T} exp\left(\frac{-169C}{100}\right)\right]. \tag{14}$$

Einstein was the pioneer in theoretical physics who first discovered the viscosity of the suspension μ_0. This formula is designed to accurately describe the viscosity of the suspension in the fluid up to a value of C = 0.6.
Radiative heat transport plays a crucial function in high-temperature systems. Typically, it is characterized using the concept of optical depth, which refers to the distance a photon travels before undergoing any changes. A liquid is considered optically thin when its penetration depth is less than one and the density of the fluid is relatively low, allowing photons to travel a considerable distance. The expression for radiative heat flux is given by Rosseland's approximation (k).

$$\frac{\partial q_r}{\partial \eta} = \frac{-16\sigma}{3k} \frac{T_0^{*3}\partial^2(T_\infty^*)}{\partial \eta^2}. \tag{15}$$

Thus, it is used to simulate the radiation component of heat transfer without the need for an additional transport equation for incident radiation.

Quantities that determine the dimensionless form of governing equations are:

$$\xi = \frac{\xi^*}{\lambda},\ \eta = \frac{\eta^*}{\tilde{a}},\ U_f = \frac{u_f^*}{\tilde{c}},\ U_p = \frac{u_p^*}{\tilde{c}},\ V_f = \frac{v_f^*\lambda}{\tilde{a}\tilde{c}},\ V_p = \frac{v_p^*\lambda}{\tilde{a}\tilde{c}},\ P = \frac{\tilde{a}^2 P^*}{\mu\tilde{c}\lambda},$$

$$\theta_f = \frac{T_f^* - T_0^*}{T_\infty^* - T_0^*},\ \theta_p = \frac{T_p^* - T_0^*}{T_\infty^* - T_0^*},\ \sigma_f = \frac{K_f^* - K_0^*}{K_\infty^* - K_0^*},\ \sigma_p = \frac{K_p^* - K_0^*}{K_\infty^* - K_0^*},\ h = \frac{H^*}{\tilde{a}},\ t = \frac{\tilde{c}t^*}{\lambda},\ N = \frac{\mu\zeta}{\tilde{a}^2},$$

$$M = \sqrt{\frac{\sigma^*}{\mu}}\beta_0\tilde{a},\ Ec = \frac{\tilde{c}^2}{(T_\infty^* - T_0^*)c_p},\ Pr = \frac{\mu c_p}{K},\ Sc = \frac{D_m\rho_f}{\mu},\ Gr = \frac{\rho g\beta_T\tilde{a}^2(T_\infty^* - T_0^*)}{\mu},$$

$$Sr = \frac{D_m\rho_f K_T}{\mu T_0^*}\left(\frac{T_\infty^* - T_0^*}{K_\infty^* - K_0^*}\right),\ Rn = \frac{16\sigma T_0^{*3}}{3kK},\ E^* = \frac{E\mu}{\rho\tilde{a}^2},\ \delta = \frac{\tilde{a}}{\lambda},\ Re = \frac{\rho\tilde{a}\tilde{c}}{\mu}. \tag{16}$$

3 Solution methodology

Under the assumptions of a long wavelength $\delta << 1$ and a low Reynolds number, the terms of order δ and above are neglected, resulting in the simplified form of equations.The mutated coupled equations from Eqs. (2)-(9) according to the alteration of non-dimensional parameters.
Succeeding Fluid phase Eqs. (17)-(20),

$$\frac{\partial P}{\partial\xi} = \left(1 + \frac{1}{\beta^*}\right)\left(\frac{\partial^2 U_f}{\partial\eta^2}\right) - \frac{C\zeta}{(1-C)}(U_f - U_p) - M^2 U_f + Gr\theta_f sin\alpha, \tag{17}$$

$$\frac{\partial P}{\partial\eta} = 0, \tag{18}$$

$$\left(\frac{\partial^2\theta_f}{\partial\eta^2}\right) + \frac{CEc\zeta Pr}{(1-C)}\left(U_f - U_p\right)^2 + \frac{Rn}{1-C}\left(\frac{\partial^2\theta_f}{\partial\eta^2}\right) = 0, \tag{19}$$

$$\frac{1}{Sc}\left(\frac{\partial^2\sigma_f}{\partial\eta^2}\right) + Sr\left(\frac{\partial^2\theta_f}{\partial\eta^2}\right) - E\sigma_f = 0. \tag{20}$$

Succeeding Particle phase Eqs. (21)-(23),

$$\frac{\partial P}{\partial\xi} = -\zeta\left(U_p - U_f\right), \tag{21}$$

$$\theta_f = \theta_p, \tag{22}$$

$$\sigma_f = \sigma_p. \tag{23}$$

Implementation of stream function $\left(U_{f,p} = \frac{\partial \psi}{\partial \eta}, V_{f,p} = -\frac{\partial \psi}{\partial \xi}\right)$ and removal of pressure imposed by Eqs. (17) and (18) gives

$$(1-C)\zeta\left(1+\frac{1}{\beta^*}\right)\frac{\partial^4\Psi}{\partial\eta^4} - M^2\zeta\frac{\partial\Psi}{\partial\eta} + Gr\frac{\partial\theta_f}{\partial\eta}\zeta sin\alpha = 0. \tag{24}$$

4 Non-dimensional boundary conditions

The nonlinear boundary value problem, as described by Eqs. (17)-(23) in its original form, can be efficiently resolved using exact mathematical techniques. Furthermore, this entails precise data for each distinct attribute of both the fluid and the particles are given in Eqs. (25) and (26).

$$\Psi = 0,\ \frac{\partial\Psi}{\partial\eta} = 0,\ \frac{\partial\theta_{f,p}}{\partial\eta} = 0,\ \frac{\partial\sigma_{f,p}}{\partial\eta} = 0, \quad at\ \ \eta = 0, \tag{25}$$

$$\Psi = \frac{F}{2},\ \frac{\partial\Psi}{\partial\eta} = 0,\ \theta_{f,p} = 1,\ \sigma_{f,p} = 1, \quad at \quad \eta = h. \tag{26}$$

Here the transformed wall equation is mentioned as

$$h = 1 + L + d\sin 2\pi\left[\xi - t\right],$$

where

$$L = \frac{\tilde{K}\xi^*}{\tilde{a}},\ d = \frac{\tilde{b}}{\tilde{a}} < 1.$$

Eq. (26) is used to find the wavy wall shear stress in terms of skin-friction coefficient C_f. Eq. (27) determines the thermal flux, which is a measure of the rate of heat exchange.
The skin friction parameter on the wall is defined as

$$C_f = \left(1+\frac{1}{\beta^*}\right)\left(\frac{\partial^2\Psi}{\partial\eta^2}\right), \quad at \quad \eta = h = 1 + L + d\sin 2\pi\left[\xi - t\right]. \tag{27}$$

The local Nusselt number parameter (Nu) is defined as

$$Nu = -\left(\frac{\partial\theta_f}{\partial\eta}\right) \quad at \quad \eta = h = 1 + L + d\sin 2\pi\left[\xi - t\right]. \tag{28}$$

The Sherwood number (Sh) is the expression of the Eq. (28) that controls the rate of mass transfer through the ureteral wall.

$$Sh = -\left(\frac{\partial\sigma_f}{\partial\eta}\right), \quad at \quad \eta = h = 1 + L + d\sin 2\pi\left[\xi - t\right]. \tag{29}$$

5 Exact solutions

The present work provides a discussion of the solutions for analytical stream function, velocity, temperature, and concentration. The Matlab allows us to solve the system of Eqs. (17)-(22) with boundary conditions (25), (26) and obtain accurate values for the stream function Ψ, velocity $\left(U_f, U_p\right)$, temperature ($\theta_{f,p}$) and concentration ($\sigma_{f,p}$). Listed below (30)-(34) are the solutions:

$$\begin{aligned}\Psi &= C_1 + C_2 e^{y\left(\frac{M^2\zeta}{(1-C)\zeta(1+1/\beta^*)}\right)^{1/3}} + C_3 e^{-\frac{y(1+\sqrt{3})\left(\frac{M^2\zeta}{(1-C)\zeta(1+1/\beta^*)}\right)^{1/3}}{2}} \\ &\quad + C_4 e^{-\frac{y(-1+\sqrt{3})\left(\frac{M^2\zeta}{(1-C)\zeta(1+1/\beta^*)}\right)^{1/3}}{2}} + \frac{Gr\zeta sin\alpha\frac{(2T_1h^2+(dP/d\xi)T_2h^2)}{2T_1h}}{M^2\zeta},\end{aligned} \tag{30}$$

$$U_f = -\frac{e^{\frac{2M^2h}{\sqrt{(1-C)\zeta(1+1/\beta^*)}}}((dP/d\xi)T_1 + GrT_2sin\alpha)(L_3 - L_2 + L_3L_1 - L_1L_2)}{M^2T_1(e^{\frac{2M^2h}{\sqrt{(1-C)\zeta(1+1/\beta^*)}}} + 1)}, \tag{31}$$

$$U_p = -\frac{e^{\frac{2M^2h}{\sqrt{(1-C)\zeta(1+1/\beta^*)}}}((dP/d\xi)T_1 + GrT_2sin\alpha)(L_3 - L_2 + L_3L_1 - L_1L_2)}{M^2T_1(e^{\frac{2M^2h}{\sqrt{(1-C)\zeta(1+1/\beta^*)}}} + 1)} - \frac{1}{\zeta}\frac{dP}{d\xi}, \tag{32}$$

$$\theta_{f,p} = \frac{y(T_2h^2 - T_2yh + 2T_1)}{2T_1h}, \tag{33}$$

$$\begin{aligned}\sigma_{f,p} &= \frac{e^{((y\sqrt{Sc}\sqrt{E})-1)}(Sr + T_1E - e^{-(\sqrt{Sc}h\sqrt{E})}Sr + (dP/d\xi)SrT_2 - (dP/d\xi)SrT_2e^{-(h\sqrt{Sc}\sqrt{E})})}{2T_1sinh(h\sqrt{Sc}\sqrt{E})} \\ &\quad - \frac{e^{((-y\sqrt{Sc}\sqrt{E})-1)}(Sr + T_1E - e^{(\sqrt{Sc}h\sqrt{E})}Sr + (dP/d\xi)SrT_2 - (dP/d\xi)SrT_2e^{(h\sqrt{Sc}\sqrt{E})})}{2T_1sinh(h\sqrt{Sc}\sqrt{E})} \\ &\quad - \frac{Sre^{-1} + (dP/d\xi)SrT_2e^{-1}}{T_1}.\end{aligned} \tag{34}$$

6 Results and discussions

We conducted measurements in this part to evaluate the impact of different conditions on the phenomenon under analysis. The parameters considered in this study encompass the Hartmann number (M), Prandtl number (Pr), Casson fluid parameter (β^*), Suspension parameter (ζ), particle volume fraction (C), Eckert number (Ec), Soret number (Sr), Schmidt number (Sc), Grashof number (Gr) as well as profiles of velocity, temperature, and concentration. The impacts of these characteristics are depicted in Figure 2 to Figure 17, complemented by an in-depth analysis. The present section is divided into three subcategories, whereby the initial subcategory is dedicated to the analysis of axial dimensionless velocity profiles under varying parameters. The next subsection presents an analysis of the effects of different parameters on the dimensionless temperature and

concentration profiles, respectively.

Flow characteristics

Figure 2 shows the drastic declination behaviour given by the Hartmann number (M) with respect to the velocity of the fluid and particle respectively. The major reason for the downswing of both the movement of urological and particles is due to the creation of Lorentz force in electrically conducting non-Newtonian fluids. The influence of a magnetic field which is mentioned in Eq. (17) as $-M^2U_f$ causes the fluid to flow with high velocity while decreasing the Hartmann number. The velocity of urological flow is hindered by the increased drag or resistance caused by the magnetic field. Slowing down the flow of urine with a magnetic field could potentially aid in controlling the movement of kidney stones. A decrease in urine flow rate could hinder the quick passage of stones through the ureter, hence lowering the likelihood of painful obstructions or acute renal colic. Figure 3 illustrates the diminishing trend of the velocity profile of particles as the Hartmann number varies. Due to the inclination of the magnetic effect, particle velocity gets reduced which helps the patients to get rid of discomfort. The risk of long-term injury to the ureter may be mitigated by a slower velocity of both urological fluid and particles, which could help prevent these issues. The axial velocity profile varies with the inclination (α), as depicted in Figure 4. As the numbers increase, there is a clear enhancement in the axial velocity profile. The results also indicate that the horizontal tube exhibits the minimum axial velocity ($\alpha = 0$), whereas the vertical tube displays the maximum axial velocity ($\alpha = \pi/3$). The importance of determining the axial velocity distribution along the ureter is emphasized by these observations, which underscore the influence of the inclination angle on the fluid flow. Figure 5 depicts various values of the Casson fluid parameter (β^*) with velocity of urological fluid. This demonstrates the amplifying behaviour. Biological fluids, such as urine, can be represented as Casson fluids because of their intricate composition, which consists of suspended cells, proteins, and other particles that contribute to the fluid's non-Newtonian characteristics. If the pressure or stress exerted on the fluid (urine) exceeds the yield stress by a large margin, the fluid can begin to flow with greater ease. Once the flow commences, the speed may escalate swiftly if the system can generate sufficient pressure to surpass the heightened resistance. Therefore, when enough pressure is exerted, raising the Casson fluid parameter may lead to a counterintuitive outcome resulting in a greater flow velocity once the fluid is set in motion. Figure 6 picturizes the velocity of particle affected by varying Casson fluid parameter (β^*). When the yield stress is exceeded by an increase in the Casson fluid parameter, the fluid will exhibit enhanced flow, leading to accelerated movement near the ureter's boundaries. In such instances, particles (such as microliths) may become entrained in these rapidly moving flow regions, leading to an enhancement in their velocity.

Figure 7 illustrates the properties of the velocity profile in relation to the heat Grashof number (Gr). Higher values of the thermal Grashof number indicate a significant temperature difference, resulting in an increased buoyant force that drives the movement of the fluid. The fluid encounters a more substantial buoyant force towards the centre as a result of elevated temperatures, whereas the force exerted at the wall is relatively diminished, which is clarified by Hosham et al. [39]. A higher Grashof number would intensify the natural convection occurring in the urine. If there are temperature gradients in the ureter or adjacent tissues, the enhanced buoyancy forces would cause the urine to travel faster, hence increasing its velocity. Figure 8 demonstrates that as the volume fraction density of the particles (C) increases, there is a noticeable decrease in the velocity of the fluid phase. This characteristic is mostly associated with the density of particles rather than their physical dimensions. Remarkably, the profiles remain consistent with the parabolic case even when C reaches high values, despite being adjusted. As the concentration of particles in the

urine increases, the viscosity of the urine likewise increases. The heightened viscosity directly leads to a reduction in the speed of urine flow. The change in velocity response when the Saffman suspension parameter (ζ), is adjusted which is depicted in Figure 9. A force that acts on small particles suspended in a fluid flow owing to the velocity gradient (shear) in the fluid is known as the Saffman suspension parameter (or Saffman lift force). This parameter is present in the momentum Stokes number, $N = \frac{\mu\zeta}{\tilde{a}^2}$ and is involved in the coupling term between the fluid phase and the particulate phase, $-\frac{C\zeta}{(1-C)}(U_f - U_p)$, in the momentum equation of the fluid phase (Eq. (17)). In contrast to the Lorentzian drag term, the coupling term acts as a supportive force on the body, and an increase in the parameter (ζ) results in more sliding between the urological fluid and particles, leading to an acceleration in the fluid phase. Particles are more likely to be elevated from the ureteral walls and into the faster-moving central region of the urine stream as the Saffman lift force increases. The flow can be optimised by relocating particulates from the walls, thereby minimising turbulence and friction. The Saffman effect, by preventing particles from sticking to the walls of the ureter, can aid in avoiding the development of blockages that may impede or obstruct the flow of urine, thereby ensuring higher velocities of flow are maintained.

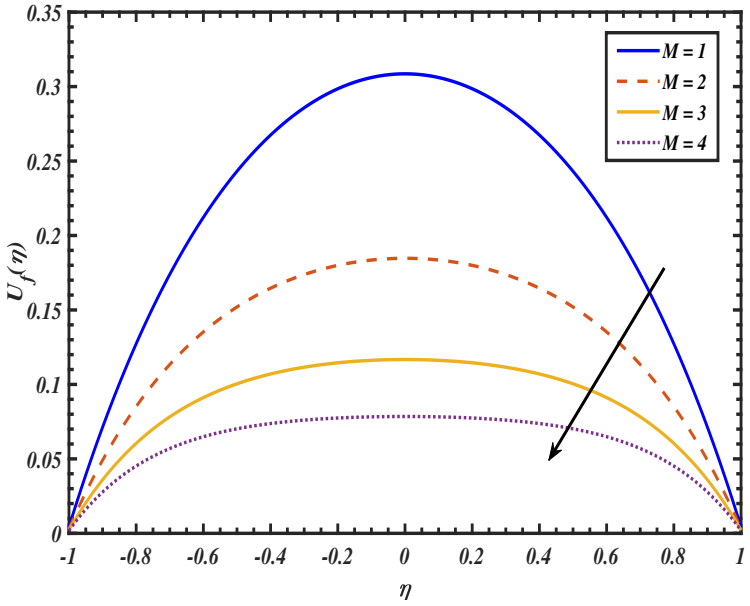

Figure 2. Influence of Hartmann number (M) on Velocity $\left(U_f\right)$

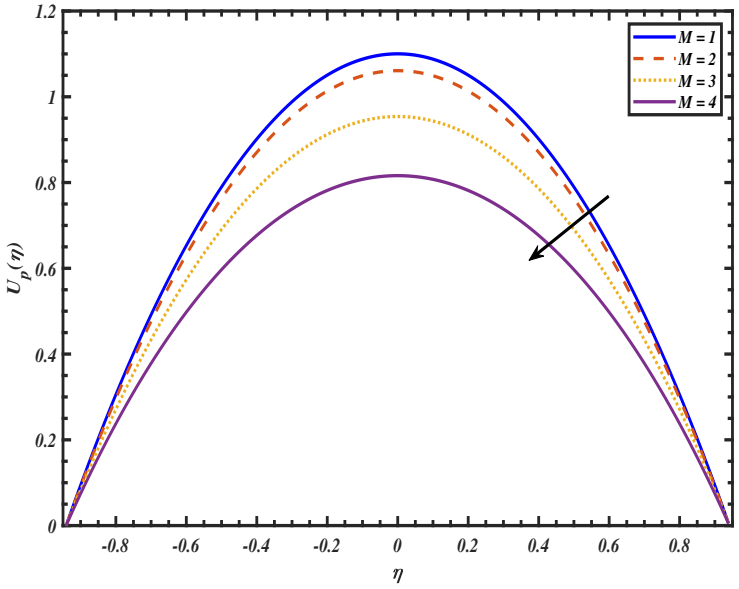

Figure 3. Influence of Hartmann number (M) on Particle Velocity (U_p)

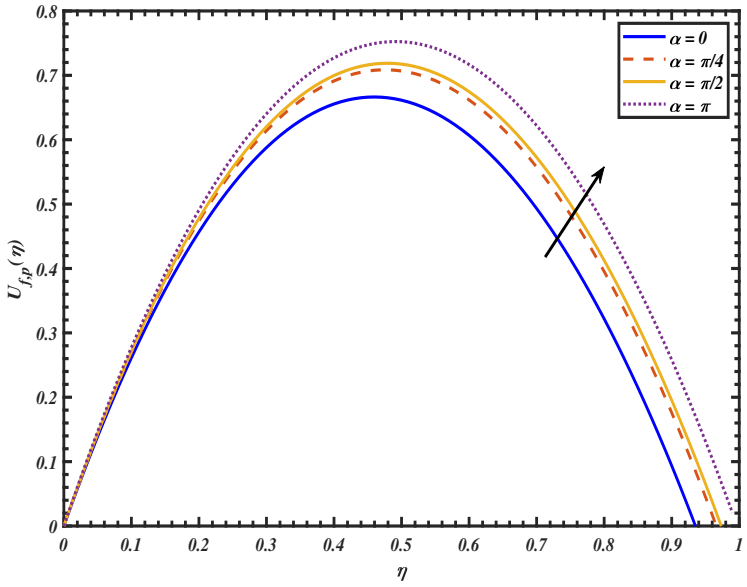

Figure 4. Influence of Inclined angle (α) on Velocity $\left(U_{f,p}\right)$

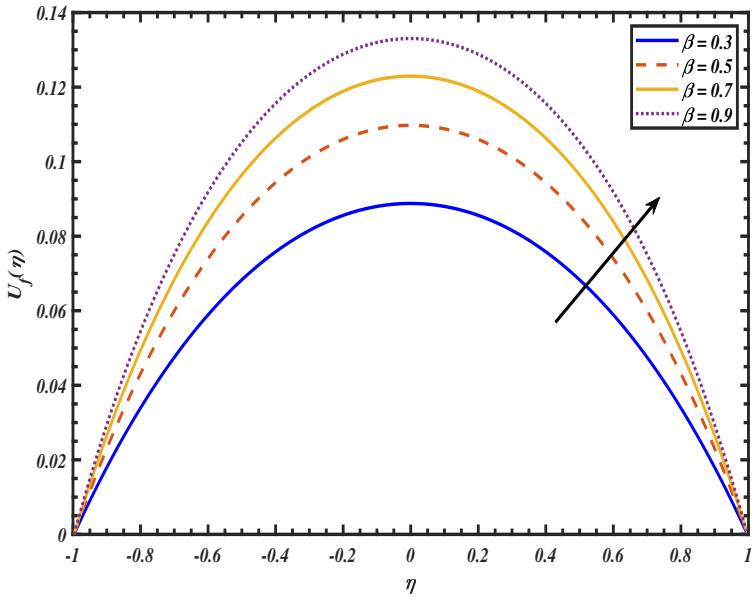

Figure 5. Influence of Casson fluid parameter (β) on Velocity $\left(U_f\right)$

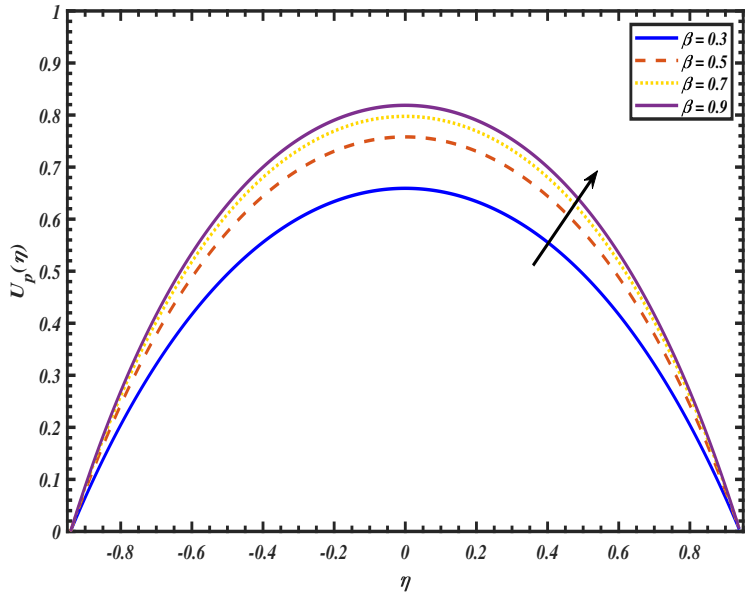

Figure 6. Influence of Casson fluid parameter (β) on Velocity $\left(U_p\right)$

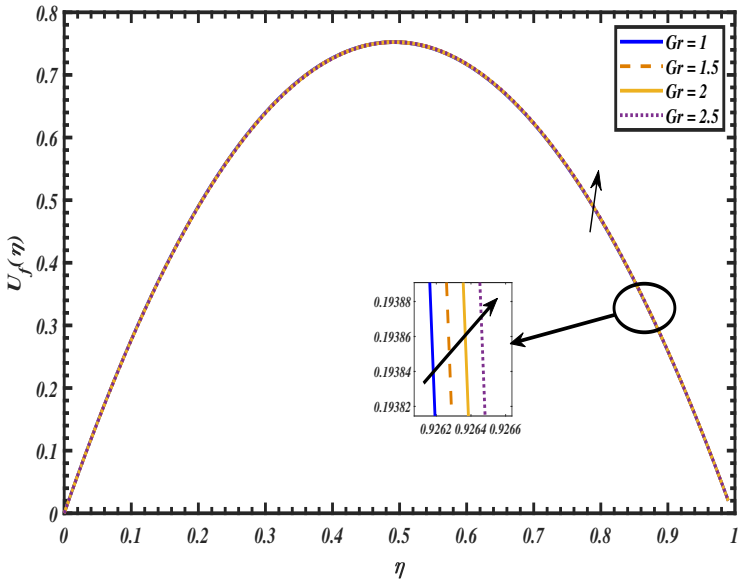

Figure 7. Influence of Grashof number (Gr) on Velocity $\left(U_f\right)$

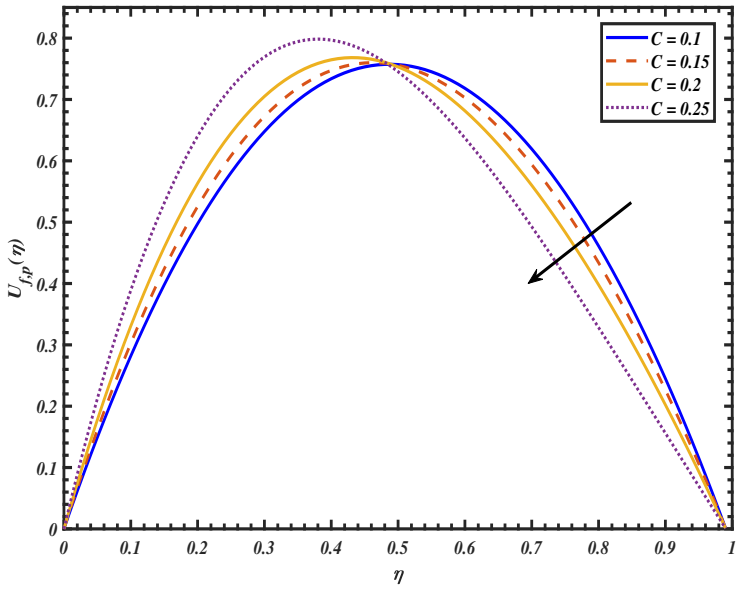

Figure 8. Influence of Particle volume fraction (C) on Velocity $\left(U_f\right)$

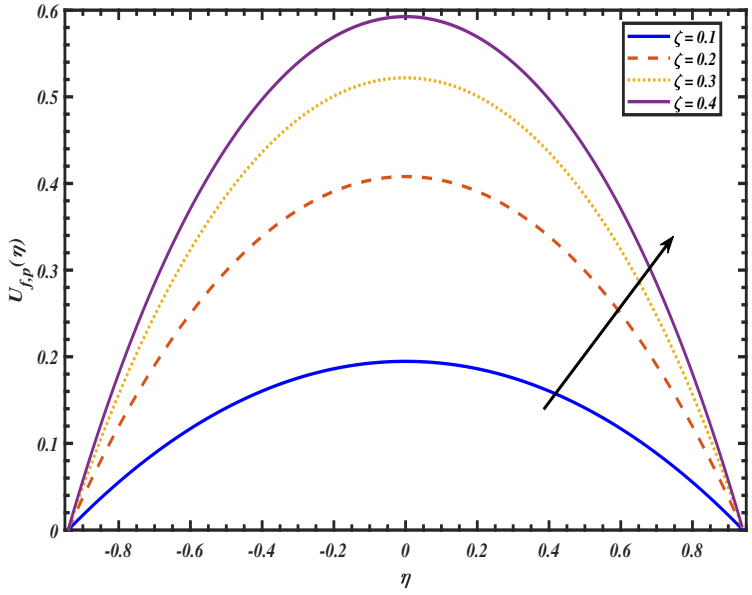

Figure 9. Influence of Suspension parameter (ζ) on Velocity $\left(U_f\right)$

Temperature profile

Figure 10 is calculated by using diverse points of the Prandtl number (Pr) to show the impact on temperature. This figure shows a flawless variation in the temperature of the fluid. The prominent behaviour of the Prandtl number gives the relation between momentum diffusivity and thermal diffusivity. The obtained graph clarifies the favourable retrogression of momentum diffusivity when magnifying the temperature rate. The Prandtl number of urine may fluctuate as a result of alterations in its composition, including variations in viscosity or thermal properties caused by dehydration, specific drugs, or nutritional variables. Figure 11 clearly demonstrates that as the thermal radiation parameter (Rn) increases, the temperature profile decreases.As the value of (Rn) gradually rises, the efficiency of energy transmission via electromagnetic waves improves, while the efficiency of thermal conduction diminishes. The latter significantly influences heat diffusion within the specified range. The comparable radiation range [40], characterised by ($Rn < 1$), is generally connected here. Diffusion heat transfer transpires due to the random motion of molecules. When this movement is suddenly diminished, adjacent molecules display reduced kinetic activity and consequently transfer energy less effectively among themselves. Augmenting the radiation parameter improves the system's ability to dissipate heat from the designated area, thereby potentially mitigating the risk of thermal damage. Thus, regulating the radiation parameter is essential for maintaining a safe and controlled environment during thermal treatments. Moreover, Figure 12 manifests the consequences of the Eckert number (Ec) on the temperature parameter. Internal friction happens mainly because of the deformation of the fluid. The molecules of the fluid move past each other. This might be the reason for the conversion of energy within a fluid. Internal friction alters the viscosity of the fluid, which also results in temperature changes. Thus, a hike in the viscosity of the fluid leads to temperature enhancement. The Eckert number is a dimensionless quantity that quantifies the ratio of kinetic energy to thermal energy. As the Eckert number increases, the conversion of the energy associated with the flow of urine into internal energy (heat) becomes more efficient due to viscous forces. As the urine passes through the ureter or other sections of the urinary tract, its temperature

rises. Understanding the detailed relationship between temperature distribution and suspension parameter (ζ) requires a graphical representation, which is illustrated in Figure 13. As the suspension parameter increases, an increased number of particles in the flow generates additional shear forces between the fluid and the particles. The shear forces induce frictional heating, thereby augmenting the total heat generation within the fluid. This phenomenon generally results in a temperature elevation, particularly in areas with elevated shear stresses, such as adjacent to the ureter walls or surrounding microliths.

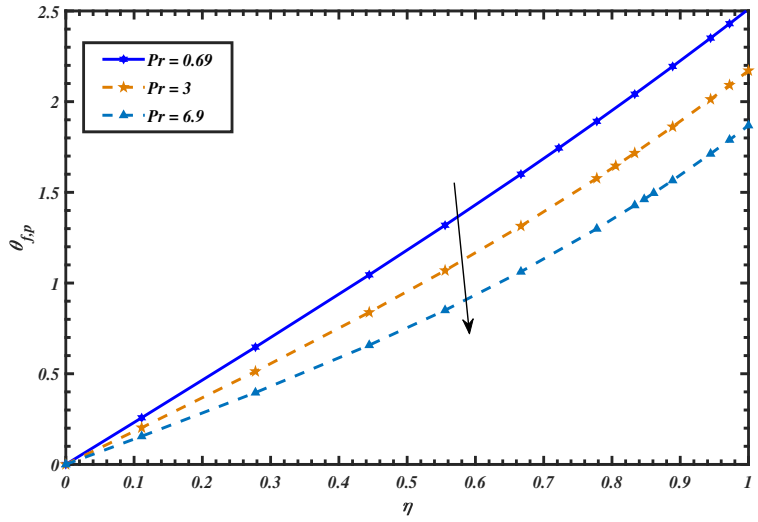

Figure 10. Influence of Prandtl Number (Pr) on Temperature $\left(\theta_{f,p}\right)$

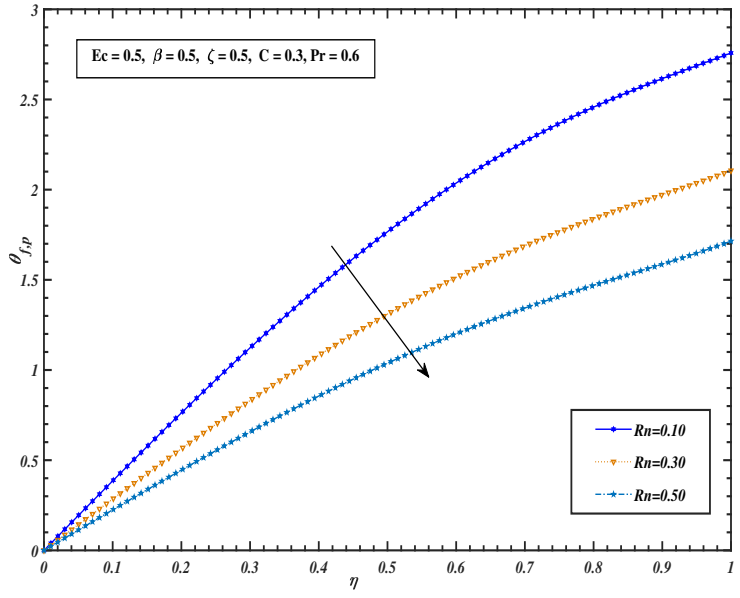

Figure 11. Influence of Thermal radiation Rn on Temperature $\left(\theta_{f,p}\right)$

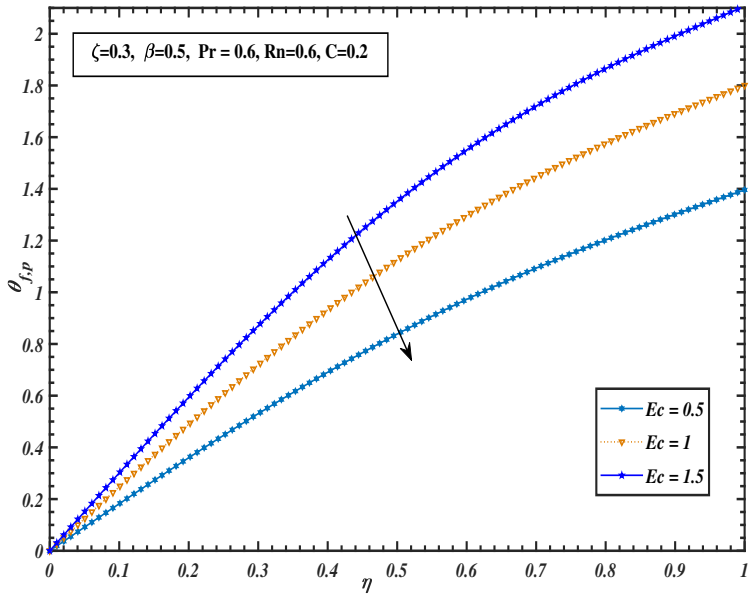

Figure 12. Influence of Eckert number Ec on Temperature $\left(\theta_{f,p}\right)$

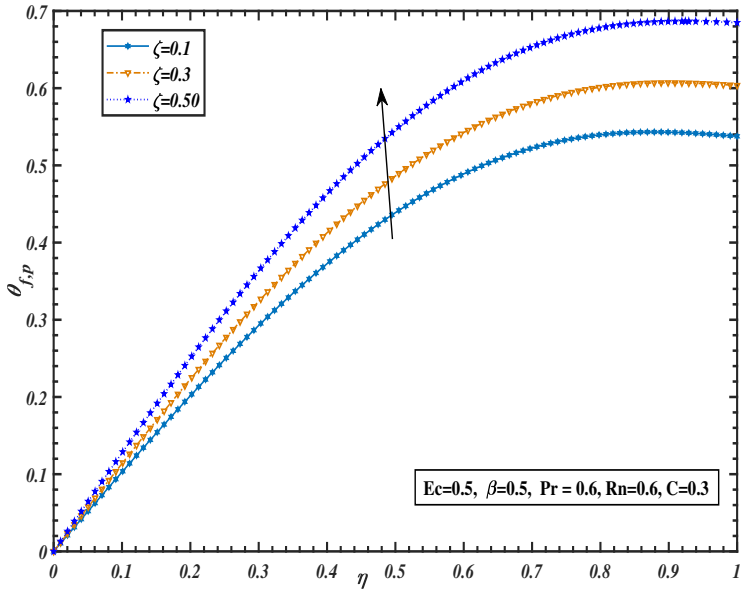

Figure 13. Influence of Suspension parameter (ζ) on Temperature $\left(\theta_{f,p}\right)$

Concentration profile

Figure 14 determined that the chemical reaction parameter (E) has a direct influence on the concentration profile. Specifically, an increase in chemical reactions results in a drop in the concentration of the species in the fluid. The concentration of the substance being transported can affect the Schmidt number (Sc) indirectly through its impact on mass diffusivity, which is figured out in Figure 15. The Schmidt number is employed as a means of quantifying the relative rates of mass diffusion and momentum diffusion inside a fluid flow. A high Schmidt

number signifies that the rate of momentum diffusion is greater than that of mass diffusion. Hence, the concentration mismatches the Schmidt number variations. A similar effect on the concentration profile is noticed for the Soret number (Sr). When the Soret number has a value that is increasing from zero, it indicates that thermal diffusion is the dominant mechanism. Figure 16 demonstrates the concentration profile for various values of the Soret number. An elevated Soret number may result in non-uniform concentration distributions along the ureter, exhibiting greater concentrations at specific locations. This enhancement of Soret number within ureteral flow enhances the migration of solute molecules, resulting in localised concentration increases that may facilitate stone formation. The term "concentration" in the context of peristaltic flow often pertains to the existence of solutes or particles inside the fluid that is undergoing flow. The distribution of concentration within the tube may exhibit variations due to the influence of mixing and transport phenomena. This effect is observed in Figure 17 as diminishing behaviour in the fluid concentration profile when enhancing the values of particles (C). The correlation between particle concentration and particle volume fraction is contingent upon the characteristics of both the particles and the fluid in which they are immersed. As the particle volume fraction increases, the available volume of fluid (urine) diminishes due to a greater proportion of the total volume being occupied by particles. Therefore, an increase in particle volume fraction leads to a reduction in the effective concentration of the fluid. A greater proportion of the fluid volume is occupied by solid particles, thereby diminishing the quantity of liquid available to transport the solutes.

Pressure gradient

In Figure 18, the pressure gradient dramatically decreases as the particle suspension parameter ζ is varied, and in Figure 19, with $\tilde{a} = 0.5$, $\tilde{b} = 0.5$, $d = 1$, and $C = 0.6$, the pressure gradient is significantly increased due to the accelerating values of (M). The lack of a reverse pressure gradient is indicated by the fact that all ξ values in these figures have positive values of $(dP/d\xi)$. This characteristic is a crucial aspect of peristaltic pumping and greatly contributes to improving the effectiveness of EMHD micropumps in medical usage. The magnetic field enhances the peristaltic flow, resulting in notable alterations in pressure distributions as a result of the inverse correlation between velocity and pressure.

Trapping phenomena plots

Trapping is another intriguing occurrence in peristaltic motion. It involves the creation of a closed system of fluid flow, resulting in the generation of a circulating bolus of fluid. Figure 20 depicts the flow patterns for various levels of Magnetic field strengths (M). It is evident that the size of the trapped bolus decreases when a magnetic field is applied. Figure 21 displays the streamlines corresponding to various Casson fluid parameter β^* with other values are choosen as $\eta = 0.1$, $d = 0.1$, $t = 0.1$, $C = 0.3$, $M = 0.3$, $\zeta = 0.5$. Similar to the behavior of the magnetic field, it has been observed that when the Casson fluid parameter β^* increases, the size of the trapping bolus decreases in both walls. The spacing between the streamlines decreases and appears symmetrical in a tapered channel.

Isothermal plots

The isotherm patterns get more twisted as the volume fraction of the particles in the fluid goes up, as shown in Figure 22(a) and Figure 22(b). This phenomenon may be attributed, from a physical standpoint to the rising temperature of the fluid as a result of the increase in the particle volume fraction (C). Continuing from Figure 23(a) and Figure 23(b), it is possible to observe the contour of the isotherm at various thermal radiation parameters (Rn). It is possible to observe that

temperature contours are decreasing as a result of an increase in the generation of thermal energy within the system as a result of the thermal radiation phenomena. The temperature eventually reaches a stable condition after some time has passed.

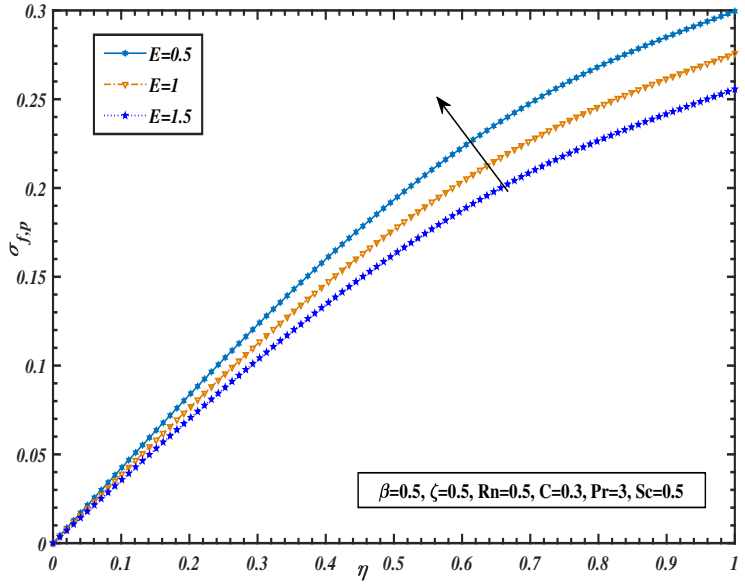

Figure 14. Influence of Chemical reaction (E) on Concentration $\left(\sigma_{f,p}\right)$

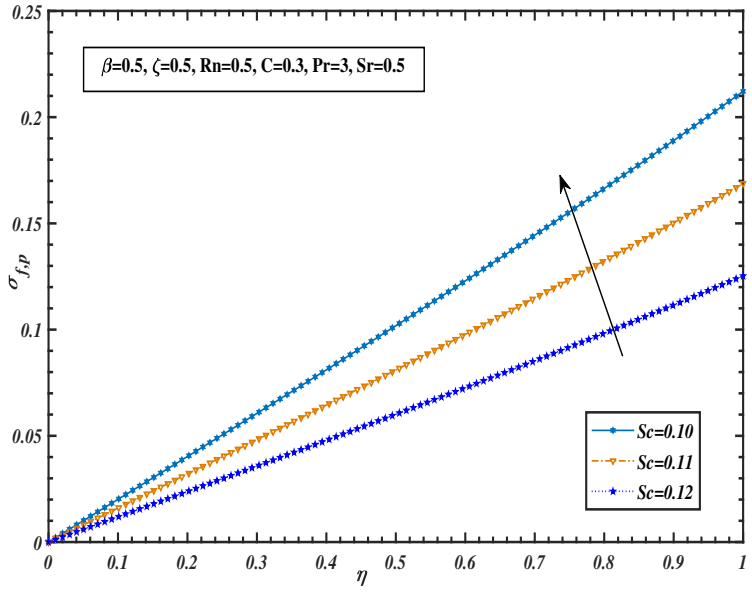

Figure 15. Influence of Schmidt number (Sc) on Concentration $\left(\sigma_{f,p}\right)$

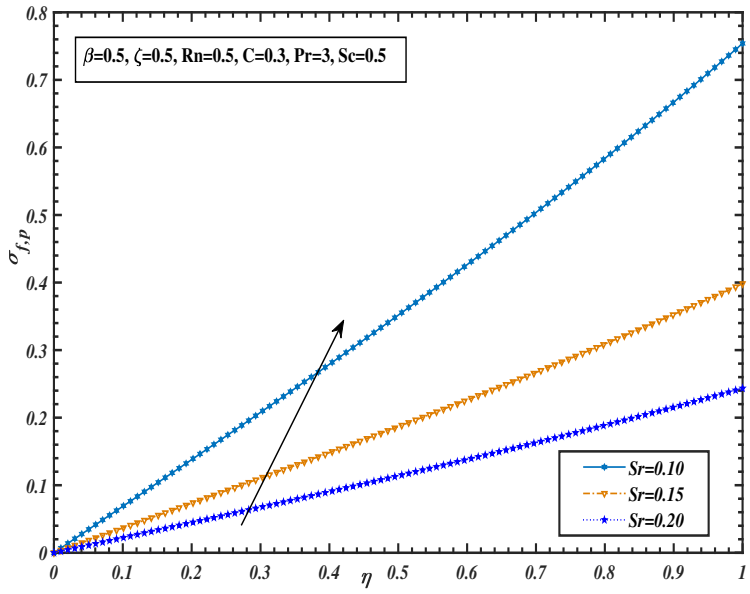

Figure 16. Influence of Soret number (Sr) on Concentration $\left(\sigma_{f,p}\right)$

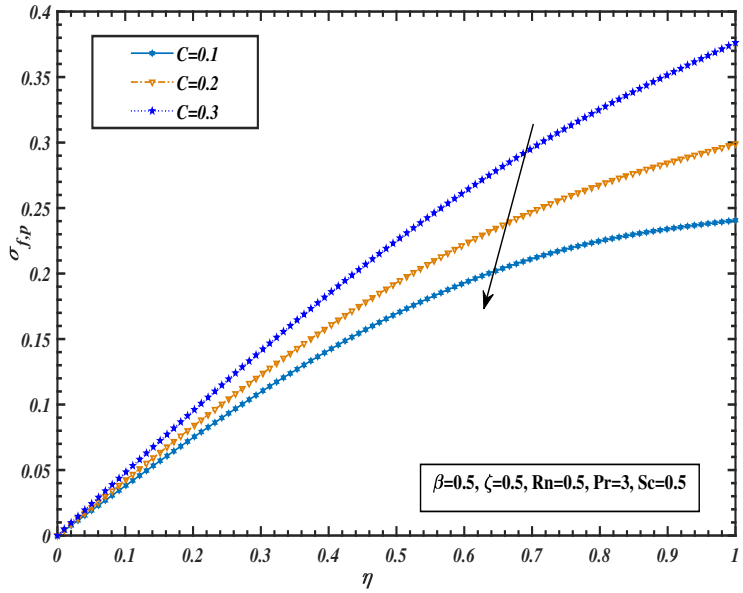

Figure 17. Influence of Particle Volume fraction (C) on Concentration $\left(\sigma_{f,p}\right)$

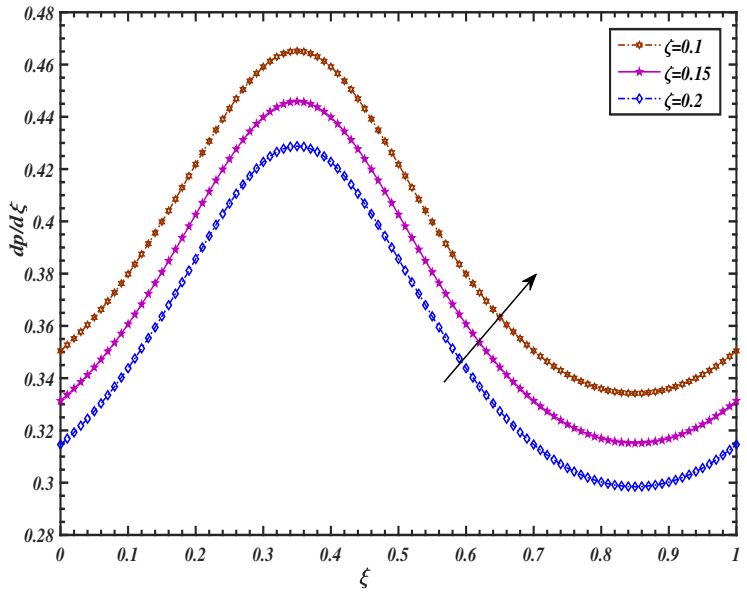

Figure 18. Impact of suspension parameter (ζ) on pressure gradient ($dp/d\xi$)

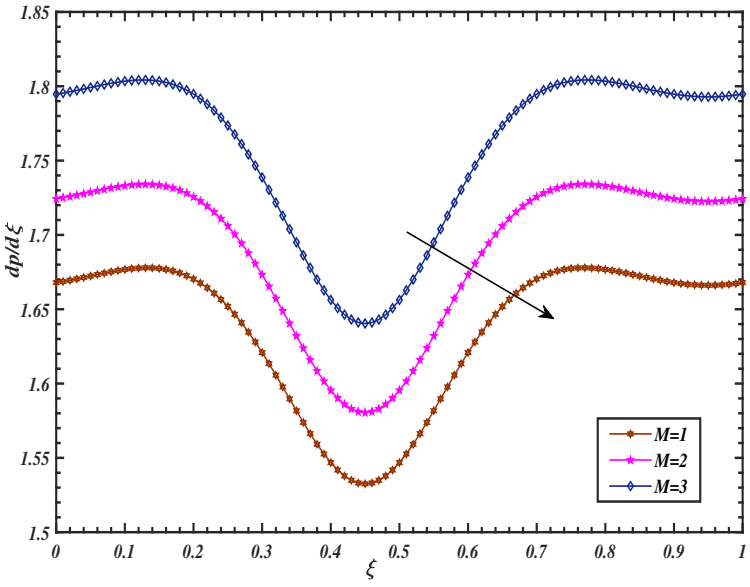

Figure 19. Impact of Magnetic field (M) on pressure gradient ($dp/d\xi$)

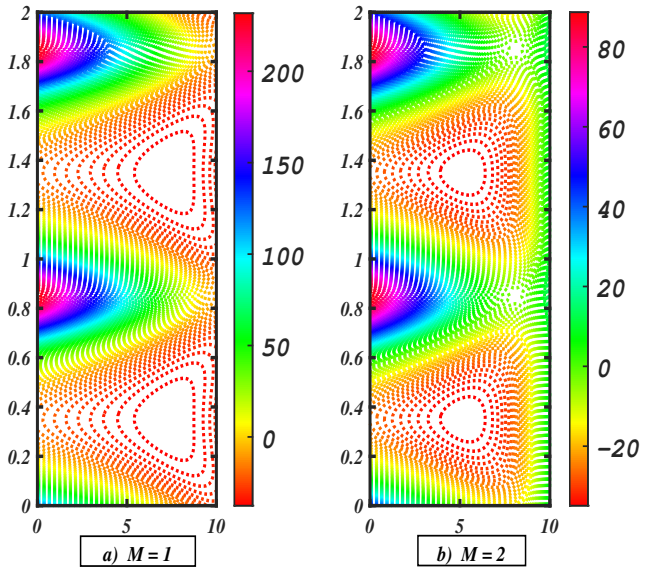

Figure 20. Streamline for various values of Magnetic field (M)

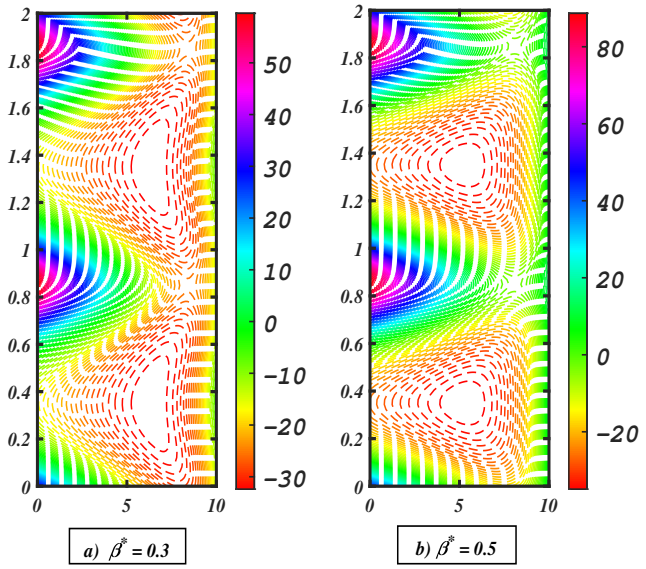

Figure 21. Streamline for various values of Casson fluid Parameter (β^*)

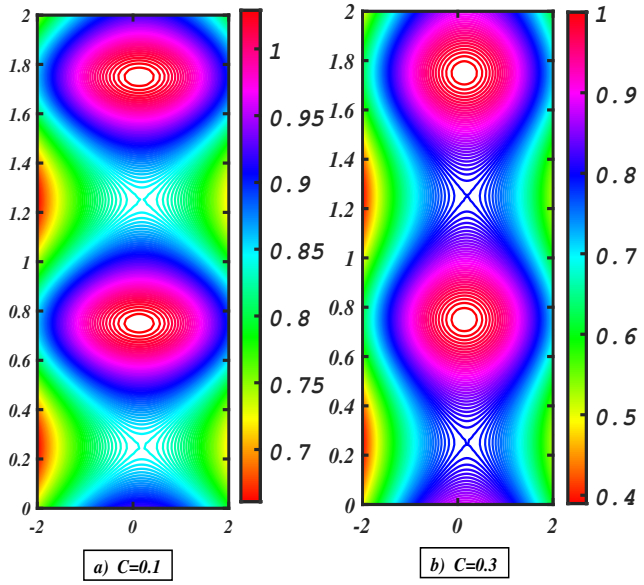

Figure 22. Isotherm plots for various values of particle volume fraction (C)

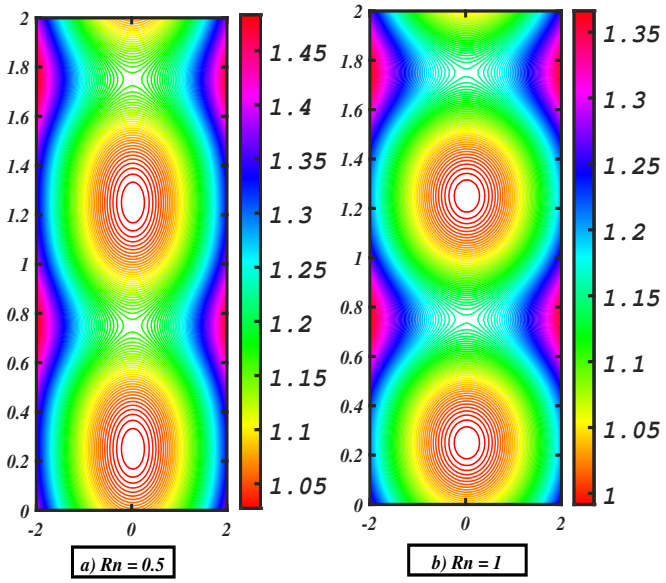

Figure 23. Isotherm plots for various values of Thermal Radiation (Rn)

Local skin friction, Nusselt number and Sherwood number

Urinary flow via ureter tube with suspension is influenced by skin friction, which provides insight into the biomedical factors that lead to kidney stone diseases. In order to improve patient outcomes, it aids in risk assessment, treatment optimisation, and the establishment of preventative programs. The connection between the skin-friction coefficient and increasing values of M, ζ, and C is positive, as can be seen from Table 1. However, an inverse relationship is shown with

increasing values of (M) and there exists a positive correlation with enhanced values of Particle volume Fraction (C). Results from Table 2 demonstrate that as the thermal radiation (Rn) increases, temperature slows down which tends the Nusselt number also get decreased. In addition to that the C, Pr, and Ec are equipped with a positive relationship with the Nusselt number. Table 3 shows the local Sherwood number for different Sc, Sr, E, and Rn combinations. In the table, you can see three different possible values for the Soret number, Sr = 0.4, 0.45 and 0.5. A higher local Sherwood number (Sh) is the result of a reduction in the speed of mass transfer, which is achieved by raising the Soret number. All across the table, for different values of the other parameter, similar observations are made. All these tables are compared with previous literature [20].

7 Validation of present work

Figure 24 displays the comparision of present work with Maraj et al. [9], with respect to Casson fluid Parameter β^* which has been verified using prior findings. The presence of a magnetic field and thermal radiation causes the flow of Casson fluid to have ongoing issues. Maraj et al. successfully addressed and studied many non-Newtonian fluids without considering the influence of thermal radiation. The present research mainly focused on thermal radiation. Based on the comparison of Maraj et al. with the present work, it is clear that the conclusions of this investigation yield strong and precise simultaneous outcomes when $Rn = 0$ in the present work.

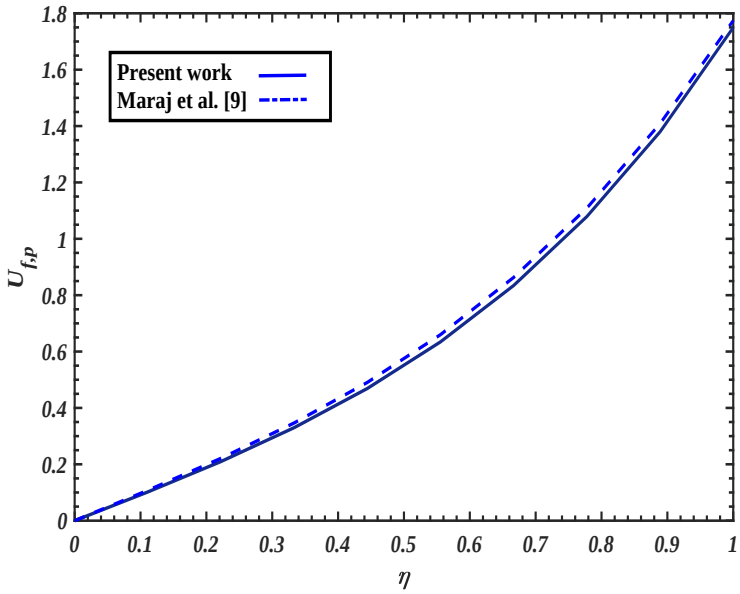

Figure 24. Validation with Maraj et al. [9] with Casson parameter (β^*)

Table 1. Comparison table of local skin friction

ζ	M	C	We	β^*	Gr	Previous study [20]	Present study
0.01	2.23	0.4	1	0.1	1.5	0.045	0.0442
0.02						0.057	0.0565
0.03						0.0675	0.0661
0.02	2.23	0.4	1	0.1	1.5	0.055	0.0558
	2					0.0892	0.0902
	3					0.0939	0.0954
0.02	1	0.05	1	0.1	1.5	0.0357	0.0353
		0.1				0.0578	0.0571
		0.2				0.0827	0.0815
0.02	2.23	0.3	1	0.1	1.5	0.0364	-
			3			0.693	-
			5			0.0875	-
0.02	2.23	0.4	1	0.1	1.5	-	0.5719
				0.2		-	0.4138
				0.3		-	0.2242
0.02	2.23	0.4	1	0.1	1	-	0.6255
					2	-	0.5146
					3	-	0.3763

Table 2. Comparison table of local Nusselt number

C	Pr	Rn	Ec	Previous study [20]	Present study
0.1	0.2	0.15	0.5	0.0768	0.0754
0.2				0.096	0.0955
0.3				0.1152	0.1158
0.3	2	0.15	0.5	0.0461	0.0458
	5			0.0691	0.0686
	7			0.1613	0.1618
0.3	0.2	0.1	0.5	-	0.5268
		0.15		-	0.4378
		0.2		-	0.3236
0.3	0.2	0.15	0.5	0.7581	0.7593
			1	0.7515	0.7521
			1.5	0.7286	0.7299

8 Conclusion

The flow through the axially symmetric pipe called the ureter, which acts as a transporter of urine from the kidney to the bladder, is dealt with in detail. From this quantitative analysis, the observation clearly explains that microlith size is highly important for the treatment of stone removal. The particles that exist in the filtration of the kidney combine to form sedimentation when it's not filtered properly. Then, if the amount of sedimentation enhances, finally tends to the stage of renal failure. The precautionary procedure for this situation is surgical intervention. To avoid those anisotropic behaviors in the wall of the ureter, a clinical visit should be the better solution when there is a struggle in the normal urine flow. Calculi inside the ureter are measured mathematically and have also emerged as mathematical models. To present a clear view of modeling, the solution process is derived numerically. There is a variety of analytical methods to decode the mathematical modeling of differential equations. This model is based on the flow inside the channel.

Table 3. Comparison table of local Sherwood number

Sc	E	Rn	Sr	Previous study [20]	Present study
0.1	0.15	0.2	0.4	0.7156	0.7199
0.2				0.6722	0.6746
0.3				0.5145	0.5178
0.15	0.1	0.2	0.4	-	0.1674
	0.2			-	0.1547
	0.3			-	0.1374
0.15	0.15	0.1	0.4	-	0.1559
		0.15		-	0.1411
		0.2		-	0.1254
0.15	0.2	0.15	0.4	0.6113	0.6126
			0.45	0.6022	0.6092
			0.5	0.5234	0.5264

* Asymptotic expressions also revealed that the flow inside the ureter is induced by long peristaltic waves.
* Graphical results disclose the interrelationships existing between velocity profile, temperature gradient, concentration, and bolus trapping when the urine is passing through the ureter with stones.
* The influence of a magnetic field causes the fluid to flow with high velocity, resulting in the downfall of the Hartmann number.
* Increasing the particle volume percentage leads to a decrease in the rate of peristaltic pumping. The presence of dispersed microparticles in the fluid medium exerts an influence on peristalsis.
* When the Prandtl values (Pr) are less than 1, the temperature change across the channel is determined by a linear profile. When the Prandtl number (Pr) is greater than 1, the temperature in the upper half of the channel experiences a substantial fall. However, this decline follows a nonlinear growth pattern that begins at a specific distance.
* A homogenous distribution of temperature across the ureter, demonstrating efficient thermal energy transmission between the urine and the ureter walls. Fluctuations in the thermal radiation parameter (Rn) indicate the existence of localised inflammation or infection, specifically known as urinary tract infections (UTIs) or inflammation of the ureter (ureteritis). As a result, the temperature inside the ureter walls rises.
* Magnetic resonance imaging (MRI) can be used to accurately establish the exact location and assess the size, shape, and composition of kidney stones before Shock Wave Lithotripsy (SWL). It also provides crucial information before, during, and after SWL.

This current research has several novel aspects of the dynamics of the ureter in two-phase conditions, which are relevant to the usage of magnetic therapy and thermal radiation techniques. These findings have potential benefits for physicians. The theoretical estimates offered here will be valuable for improving the accuracy of patient treatment and achieving more effective results in thermal therapy for pain relief. This study will also have practical uses in predicting the levels of electromagnetic radiation that a person may be exposed to when working in areas with radiation. This study, by considering heat transmission, will be useful for conducting heat-dose sensitivity tests, which are essential for the proper management of CKD.

Appendix

$$C_1 = \frac{(3M^2\zeta)(M^2\zeta^{(1/2)}Fe^{M^2\zeta^{(1/2)}h} + T_1M^2\zeta^{(1/2)}Fe^{-M^2\zeta^{(1/2)}h})T_2}{(2)(2e^{-M^2\zeta^{(1/2)}h} - 2e^{M^2\zeta^{(1/2)}h} + 2M^2\zeta^{(1/2)}he^{M^2\zeta^{(1/2)}h} + 2M^2\zeta^{1/2}he^{-M^2\zeta^{(1/2)}h} - 1)},$$

$$C_2 = \frac{(F - Fe^{(M^2\zeta^{(1/2)}h)}) + Fe^{(M^2\zeta^{(1/2)}h)} + T_2M^2\zeta^{(1/2)}Fhe^{(M^2\zeta^{(1/2)}h)} + T_1M^2\zeta^{(1/2)}Fhe^{(M^2\zeta^{(1/2)}h)}}{(2)(2e^{(-M^2\zeta^{(1/2)}h)} - 2e^{(M^2\zeta^{(1/2)}h)} + T_12M^2\zeta^{(1/2)}he^{(M^2\zeta^{(1/2)}h)} + T_22M^2\zeta^{(1/2)}he^{(-M^2\zeta^{(1/2)}h)} - 1)},$$

$$C_3 = \frac{(3F)T_1T_2}{(2)(2e^{(-M^2\zeta^{(1/2)}h)} - 2e^{(M^2\zeta^{(1/2)}h)} + T_12M^2\zeta^{(1/2)}he^{(M^2\zeta^{(1/2)}h)} + T_22M^2\zeta^{(1/2)}he^{(-M^2\zeta^{(1/2)}h)} - 1)},$$

$$C_4 = \frac{-(3F)T_1T_2}{(2)(2e^{(-M^2\zeta^{(1/2)}h)} - T_12e^{(M^2\zeta^{(1/2)}h)} + T_12M^2\zeta^{(1/2)}he^{(M^2\zeta^{(1/2)}h)} + T_22M^2\zeta^{(1/2)}he^{(-M^2\zeta^{(1/2)}h)} - 1)},$$

$$T_1 = \left(1 + \frac{Rn}{(1-C)}\right),$$

$$T_2 = \frac{CEcPr}{\zeta(1-C)},$$

$$L_1 = e^{\frac{2M^2h}{\sqrt{(1-C)\zeta(1+1/\beta^*)}}},$$

$$L_2 = e^{\frac{M^2y}{\sqrt{(1-C)\zeta(1+1/\beta^*)}}},$$

$$L_3 = e^{\frac{M^2h}{\sqrt{(1-C)\zeta(1+1/\beta^*)}}}.$$

Nomenclature

u_f^*, v_f^*	Fluid phase velocity components (m/s)	u_p^*, v_p^*	Particle phase velocity components (m/s)
$\tilde{b}$	Amplitude (m)	N	Stoke's constant
$\tilde{c}$	Constant velocity (ms^{-1})	λ	Wavelength (m)
$\tilde{K}$	Channel's length-dependent constant (m)	ζ	Suspension parameter
σ^*	Electrical conductivity of the fluid (sm^{-1})	P^*	Pressure ($Kgm^{-1}s^{-2}$)
β_0	Transverse magnetic field intensity(kg/s^2A)	t^*	Time (s)
$(\rho c_p)_f$	Specific heat capacity($J.kg^{-1}.K^{-1}$)	μ	Plastic Dynamic viscosity ($kgm^{-1}s^{-1}$)
$\tilde{a}$	Channel's half-width (m)	Re	Reynolds number
C	Particle volume fraction	M	Hartmann number
T_f^*	Fluid phase temperature (K)	T_p^*	Particle phase temperature(K)
$K_{f,p}^*$	Dimensional Fluid,Particulate concentration	ρ	Urological density (kgm^{-3})
K	Thermal conductivity ($Wm^{-1}K^{-1}$)	Sr	Soret number
β^*	Casson fluid Parameter	Sc	Schmidt number
Pr	Prandtl number	$H^*(\xi^*, t^*)$	Channel wall (m)
ξ	Non-dimensional axial coordinate (m)	h	Non-dimensional channel wall
η	Dimensionless transverse coordinate (m)	ρ_p	Particulate density (kgm^{-3})
D_m	Molecular diffusivity of the particles	Ec	Eckert number

Declarations

Use of AI tools

The authors declare that they have not used Artificial Intelligence (AI) tools in the creation of this article.

Data availability statement

No Data associated with the manuscript.

Ethical approval (optional)

The authors state that this research complies with ethical standards. This research does not involve either human participants or animals.

Consent for publication

Not applicable

Conflicts of interest

The authors declare that they have no conflict of interest.

Funding

No funding was received for this research.

Author's contributions

P.D.: Writing-Original draft preparation, Conceptualization, Methodology, Software. E.P.S.: Data curation, Formal Analysis, Investigation. K.L.: Visualization, Validation, Supervision. All authors discussed the results and contributed to the final manuscript.

Acknowledgements

Not applicable

References

[1] Lozano, J.N.J. *Peristaltic Flow with Application to Ureteral Biomechanics*. Ph.D Thesis, Department of Aerospace and Mechanical Engineering, University of Notre Dame, (2009). [CrossRef]

[2] Kiil, F. Urinary flow and ureteral peristalsis. In, *Urodynamics Upper and Lower Urinary Tract* (pp. 7-70). Heidelberg, Germany: Springer, (1973). [CrossRef]

[3] Vahidi, B., Fatouraee, N., Imanparast, A. and Moghadam, A.N. A mathematical simulation of the ureter: effects of the model parameters on ureteral pressure/flow relations. *Journal of Biomechanical Engineering*, 133(3), 031004, (2011). [CrossRef]

[4] Srivastava, L.M. and Srivastava, V.P. Peristaltic transport of a particle-fluid suspension. *Journal of Biomechanical Engineering*, 111(2), 157-165, (1989). [CrossRef]

[5] Kamel, M.H., Eldesoky, I.M., Maher, B.M. and Abumandour, R.M. Slip effects on peristaltic transport of a particle-fluid suspension in a planar channel. *Applied Bionics and Biomechanics*, 2015(1), 703574, (2015). [CrossRef]

[6] Ramesh, K., Tripathi, D., Bég, O.A. and Kadir, A. Slip and hall current effects on Jeffrey fluid

suspension flow in a peristaltic hydromagnetic blood micropump. *Iranian Journal of Science and Technology, Transactions of Mechanical Engineering*, 43, 675-692, (2019). [CrossRef]

[7] Misra, J.C. and Pandey, S.K. Peristaltic transport of a particle-fluid suspension in a cylindrical tube. *Computers & Mathematics with Applications*, 28(4), 131-145, (1994). [CrossRef]

[8] Mohd Kasim, A.R., Arifin, N.S., Mohd Zokri, S., Salleh, M.Z., Mohammad, N.F., Chuan Ching, D.L. et al. Convective transport of fluid–solid interaction: A study between non-Newtonian Casson model with dust particles. *Crystals*, 10(9), 814, (2020). [CrossRef]

[9] Maraj, E.N., Shah, S.I., Akbar, N.S. and Muhammad, T. Thermally progressive Particle-Cu/Blood peristaltic transport with mass transfer in a Non-Uniform Wavy Channel: Closed-form exact solutions. *Alexandria Engineering Journal*, 74, 453-466, (2023). [CrossRef]

[10] Riaz, A. and Sadiq, M.A. Particle–fluid suspension of a non-Newtonian fluid through a curved passage: an application of urinary tract infections. *Frontiers in Physics*, 8, 109, (2020). [CrossRef]

[11] Hayat, T., Asghar, S., Tanveer, A. and Alsaedi, A. Chemical reaction in peristaltic motion of MHD couple stress fluid in channel with Soret and Dufour effects. *Results in Physics*, 10, 69-80, (2018). [CrossRef]

[12] Zhang, L., Bhatti, M.M. and Michaelides, E.E. Thermally developed coupled stress particle–fluid motion with mass transfer and peristalsis. *Journal of Thermal Analysis and Calorimetry*, 143, 2515-2524, (2021). [CrossRef]

[13] Bhatti, M.M., Zeeshan, A., Ijaz, N., Bég, O.A. and Kadir, A. Mathematical modelling of nonlinear thermal radiation effects on EMHD peristaltic pumping of viscoelastic dusty fluid through a porous medium duct. *Engineering Science and Technology, An International Journal*, 20(3), 1129-1139, (2017). [CrossRef]

[14] Bhatti, M.M., Zeeshan, A., Asif, M.A., Ellahi, R. and Sait, S.M. Non-uniform pumping flow model for the couple stress particle-fluid under magnetic effects. *Chemical Engineering Communications*, 209(8), 1058-1069, (2022). [CrossRef]

[15] Kaimal, M.R. Peristaltic pumping of a Newtonian fluid with particles suspended in it at low Reynolds number under long wavelength approximations. *Journal of Applied Mechanics*, 45(1), 32-36, (1978). [CrossRef]

[16] Sankad, G.C. and Nagathan, P.S. Transport of MHD couple stress fluid through peristalsis in a porous medium under the influence of heat transfer and slip effects. *International Journal of Applied Mechanics and Engineering*, 22(2), 403-414, (2017). [CrossRef]

[17] Ramesh, K., Tripathi, D., Bhatti, M.M. and Khalique, C.M. Electro-osmotic flow of hydromagnetic dusty viscoelastic fluids in a microchannel propagated by peristalsis. *Journal of Molecular Liquids*, 314, 113568, (2020). [CrossRef]

[18] Hayat, T., Ayub, S., Alsaedi, A., Tanveer, A. and Ahmad, B. Numerical simulation for peristaltic activity of Sutterby fluid with modified Darcy's law. *Results in Physics*, 7, 762-768, (2017). [CrossRef]

[19] Prakash, J., Siva, E.P., Balaji, N. and Kothandapani, M. Effect of peristaltic flow of a third grade fluid in a tapered asymmetric channel. In Proceedings, *National Conference on Mathematical Techniques and its Applications (NCMTA)*, pp. 1-22, Kattankulathur, India, (2018, January). [CrossRef]

[20] Deepalakshmi, P., Siva, E.P., Tripathi, D., Bég, O.A. and Kuharat, S. MHD peristaltic two-phase Williamson fluid flow, heat and mass transfer through a ureteral tube with microliths:

Electromagnetic therapy simulation. *Numerical Heat Transfer, Part A: Applications*, 1-24, (2024). [CrossRef]

[21] Mernone, A.V., Mazumdar, J.N. and Lucas, S.K. A mathematical study of peristaltic transport of a Casson fluid. *Mathematical and Computer Modelling*, 35(7-8), 895-912, (2002). [CrossRef]

[22] Bhatti, M.M., Zeeshan, A., Tripathi, D. and Ellahi, R. Thermally developed peristaltic propulsion of magnetic solid particles in biorheological fluids. *Indian Journal of Physics*, 92, 423-430, (2018). [CrossRef]

[23] Eldabe, N.T., Abouzeid, M.Y. and Ali, H.A. Effect of heat and mass transfer on Casson fluid flow between two co-axial tubes with peristalsis. *Journal of Advanced Research in Fluid Mechanics and Thermal Sciences*, 76(1), 54-75, (2020). [CrossRef]

[24] Mekheimer, K.S., El Shehawey, E.F. and Elaw, A.M. Peristaltic motion of a particle-fluid suspension in a planar channel. *International Journal of Theoretical Physics*, 37, 2895-2920, (1998). [CrossRef]

[25] Imran, N., Javed, M., Qayyum, M., Sohail, M. and Kashif, M. Heat transfer analysis for particle–fluid suspension thermomagnetohydrodynamic peristaltic flow with Darcy–Forchheimer medium. *Heat Transfer*, 50(4), 3547-3563, (2021). [CrossRef]

[26] Kothandapani, M. and Srinivas, S. Non-linear peristaltic transport of a Newtonian fluid in an inclined asymmetric channel through a porous medium. *Physics Letters A*, 372(8), 1265-1276, (2008). [CrossRef]

[27] Prakash, J., Siva, E.P., Tripathi, D. and Bég, O.A. Thermal slip and radiative heat transfer effects on electro-osmotic magnetonanoliquid peristaltic propulsion through a microchannel. *Heat Transfer—Asian Research*, 48(7), 2882-2908, (2019). [CrossRef]

[28] Kothandapani, M. and Prakash, J. Influence of thermal radiation and magnetic field on peristaltic transport of a Newtonian nanofluid in a tapered asymmetric porous channel. *Journal of Nanofluids*, 5(3), 363-374, (2016). [CrossRef]

[29] Bhatti, M.M., Ellahi, R., Zeeshan, A., Marin, M. and Ijaz, N. Numerical study of heat transfer and Hall current impact on peristaltic propulsion of particle-fluid suspension with compliant wall properties. *Modern Physics Letters B*, 33(35), 1950439, (2019). [CrossRef]

[30] Prakash, J., Siva, E.P., Tripathi, D. and Kothandapani, M. Nanofluids flow driven by peristaltic pumping in occurrence of magnetohydrodynamics and thermal radiation. *Materials Science in Semiconductor Processing*, 100, 290-300, (2019). [CrossRef]

[31] Jiménez-Lozano, J., Sen, M. and Corona, E. Analysis of peristaltic two-phase flow with application to ureteral biomechanics. *Acta Mechanica*, 219, 91-109, (2011). [CrossRef]

[32] Prakash, J., Tripathi, D., Akkurt, N. and Bég, O.A. Tangent hyperbolic non-Newtonian radiative bioconvection nanofluid flow from a bi-directional stretching surface with electro-magneto-hydrodynamic, Joule heating and modified diffusion effects. *The European Physical Journal Plus*, 137, 472, (2022). [CrossRef]

[33] Shankar, G. and Siva, E.P. A numerical investigation of thermal and mass exchange of blood along porous stenosis arterial flow with applied magnetic field. *IAENG International Journal of Applied Mathematics*, 54(3), 532-541, (2024).

[34] Deepalakshmi, P., Darvesh, A., Garalleh, H.A., Sánchez-Chero, M., Shankar, G. and Siva, E.P. Integrate mathematical modeling for heat dynamics in two-phase Casson fluid flow through renal tubes with variable wall properties. *Ain Shams Engineering Journal*, 16(1), 103183, (2025).

[CrossRef]

[35] Eroğlu, B.B.İ. Two-dimensional Cattaneo-Hristov heat diffusion in the half-plane. *Mathematical Modelling and Numerical Simulation with Applications*, 3(3), 281-296, (2023). [CrossRef]

[36] Loganathan, K., Thamaraikannan, N., Eswaramoorthi, S. and Jain, R. Entropy framework of the bioconvective Williamson nanofluid flow over a Riga plate with radiation, triple stratification and swimming microorganisms. *International Journal of Thermofluids*, 25, 101000, (2025). [CrossRef]

[37] Sinan, M., Leng, J., Anjum, M. and Fiaz, M. Asymptotic behavior and semi-analytic solution of a novel compartmental biological model. *Mathematical Modelling and Numerical Simulation with Applications*, 2(2), 88-107, (2022). [CrossRef]

[38] Srivastava, L.M. and Srivastava, V.P. Peristaltic transport of a particle-fluid suspension. *Journal of Biomechanical Engineering*, 111(2), 157-165, (1989). [CrossRef]

[39] Hosham, H.A. and Hafez, N.M. Bifurcation phenomena in the peristaltic transport of non-Newtonian fluid with heat and mass transfer effects. *Journal of Applied Mathematics and Computing*, 67, 275-299, (2021). [CrossRef]

[40] Shankar, G., Siva, E.P., Tripathi, D. and Beg, O. A. Thermal analysis in unsteady oscillatory Darcy blood flow through stenosed artery. *International Journal of Thermofluids*, 24, 100864, (2024). [CrossRef]

Mathematical Modelling and Numerical Simulation with Applications (MMNSA)
(https://dergipark.org.tr/en/pub/mmnsa)

How to cite this article: Deepalakshmi, P., Siva, E.P. and Loganathan, K. (2024). Two-phase MHD peristaltic flow of non-Newtonian Casson fluid through the renal tube in the presence of microliths. *Mathematical Modelling and Numerical Simulation with Applications*, 4(4), 416-447. https://doi.org/10.53391/mmnsa.1536174